Front. Optoelectron. 2013, 6(1): 89–96
DOI 10.1007/s12200-012-0307-5

REVIEW ARTICLE

Stress engineering and the applications of inhomogeneously polarized optical fields

Thomas G. BROWN (✉)[1], Amber M. BECKLEY[2]

1 The Institute of Optics, University of Rochester, Rochester, NY 14627, USA
2 Department of Engineering Physics, École Polytechnique de Montréal, Montréal, QC H3C 3A7, Canada

Abstract Spatial inhomogeneities in the polarization of a light field can show fascinating effects in focusing, propagation, illumination, and imaging. This paper provides examples of these effects and describes how deterministic stress on the periphery of an optical element can be used in fundamental studies of beam propagation, as well as applications such as polarimetry.

Keywords polarization, birefringence, physical optics

1 Introduction

The last decade has seen an explosion of interest in the theory, application, and implementation of inhomogeneously polarized optical fields. These studies have included both polarization related phenomena in the paraxial regime of propagation and focusing [1], as well as the study of 3D fields in focusing systems having a very high numerical aperture [2,3, and references therein, 4–8]. It was in connection with this work that the Rochester group began a research effort directed at tailoring optical polarization through optomechanical means [9–11], in order to provide engineering options for polarization control that are both wavelength and material agile, particularly for needs in systems and wavelength ranges not well suited for liquid crystal polarization control. This paper will provide a brief introduction to the concepts of inhomogeneous polarization and stress engineering.

For the majority of the paper, we will consider fully correlated beam-like fields, whose local state of polarization may be considered fully polarized. Two popular examples that represent a significant fraction of the fields studied are shown in Fig. 1. We will refer to them by the popular designations (azimuthal and radial), recognizing that in the various of theories of electromagnetic dipole radiation, these are the beam-like approximations to transverse-electric (TE) and transverse magnetic (TM) solutions to the Helmholtz equation. As a class, they have also received the designation cylindrical vector beams indicating a polarization and phase with perfect cylindrical symmetry.

In the paraxial limit, these beams can be written as linear superpositions of other beamlike solutions. For example, two linearly polarized (LP) Hermite-Gauss modes can be superimposed as follows to form a radially polarized beam.

$$\begin{bmatrix} x \\ 0 \end{bmatrix} \mathrm{e}^{-\beta\rho^2} + \begin{bmatrix} 0 \\ y \end{bmatrix} \mathrm{e}^{-\beta\rho^2} = \begin{bmatrix} \cos\phi \\ \sin\phi \end{bmatrix} \rho \mathrm{e}^{-\beta\rho^2},$$

where $\rho^2 = x^2 + y^2$ is the normalized radial coordinate and ϕ is the polar angle.

This type of superposition can be experimentally implemented in various types of interferometers, including both Mach-Zehnder and Twyman-Green/Michelson designs. Figure 2 shows a schematic and accompanying photograph of an experimental Mach-Zehnder design implemented by Youngworth and Brown [7,8].

Azimuthal and radial beams may also be superimposed to form a LaGuerre-Gauss type beam of uniform circular polarization:

$$E = \frac{1}{2}\left(\begin{bmatrix} \cos\phi \\ \sin\phi \end{bmatrix} + \mathrm{i} \begin{bmatrix} \sin\phi \\ -\cos\phi \end{bmatrix} \right) = \mathrm{e}^{\mathrm{i}\phi} \begin{bmatrix} 1 \\ -\mathrm{i} \end{bmatrix}. \quad (1)$$

These simple examples suggest that more generalized field superpositions can readily be conceived and implemented. To generalize the picture of polarization state superposition, we make use of the Poincaré sphere formalism, in which the normalized Stokes 3-vector is represented as a point on the surface of the sphere (for fully polarized states) and within the sphere (for partially polarized states).

Received December 5, 2012; accepted December 20, 2012

E-mail: thomas.brown@rochester.edu

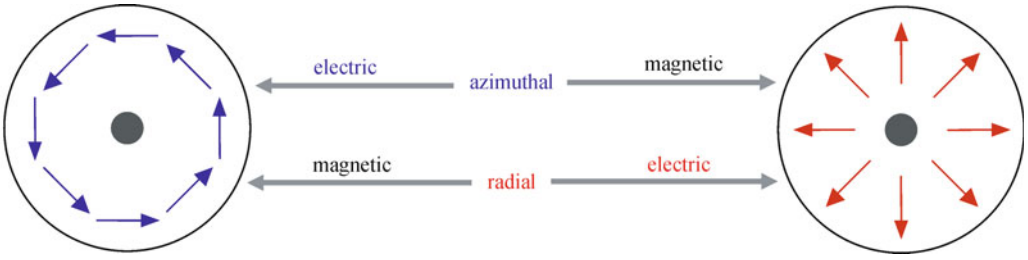

Fig. 1 Azimuthal (left) and radial (right) polarization states are locally plane-polarized in a way that retains cylindrical symmetry about the beam axis in both polarization and phase

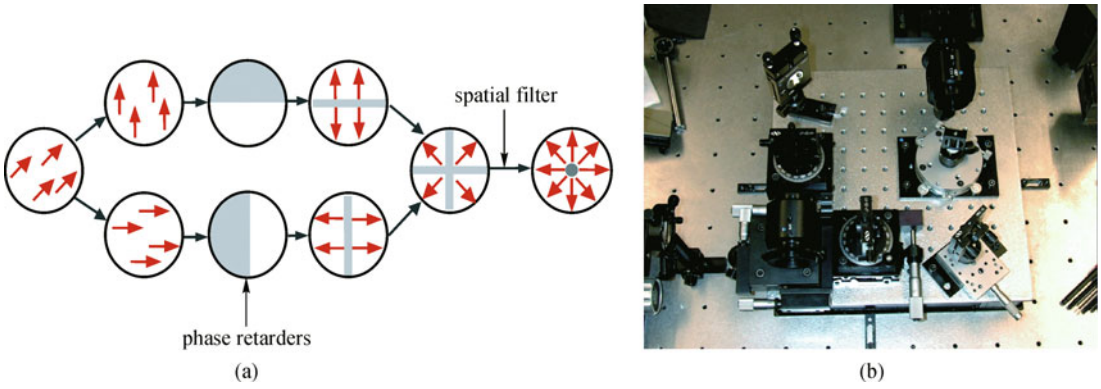

Fig. 2 Scheme (a) of Youngworth and Brown to form a cylindrical vector beam (radial illustrated here) based on Mach-Zehnder interferometer. The right hand side (b) shows a photograph of the interferometer

All of these representations approximate the optical field as a vector field that oscillates in a plane perpendicular to the direction of propagation. This accurately describes beam-like fields having a well-confined angular spectrum, but can also describe the local polarization of perfectly monochromatic fields.

Under such an approximation, one may take a generalized superposition (shown in Fig. 3), in which both the amplitude ratio of the two polarizations as well as their phase may vary from point to point over the surface of the beam. For example, if the two beams represent circularly polarized fields of equal amplitude but with a spatially varying phase, the resulting beam will occupy the equatorial region of the sphere. Two beams of equal phase will occupy a great circle (or a portion thereof) of the Poincaré sphere depending on their range of relative amplitudes.

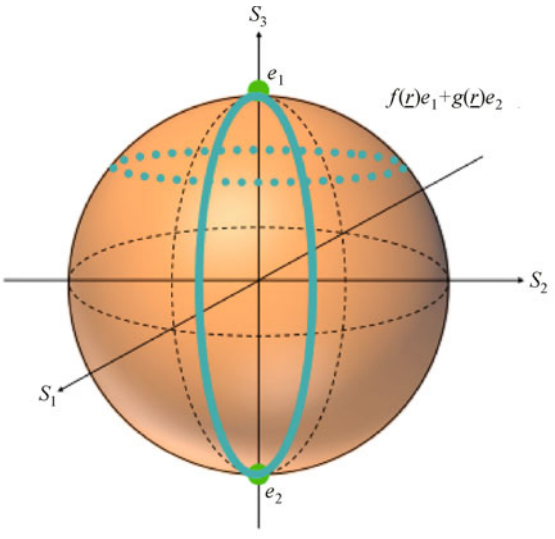

Fig. 3 Poincaré sphere representation of two polarization states superimposed with relative amplitude and phase. The phase difference determines the longitude and the relative amplitude the latitude when pictured on a sphere

2 Stress engineering

It has been known for some time that forces applied about the periphery of an optical window will induce a smoothly varying birefringence pattern, whose functional form is determined by the symmetry of the force. While it is possible to solve these sorts of generalized problems using numerical tools (e.g., finite element analysis), having analytic forms for the solution provides a helpful way of connecting the optomechanics of the window to Fourier analysis of an optical system. When the window (as is typical) is placed in the pupil plane, the window becomes a polarization apodization element.

Figure 4 shows a comparison of a finite element model

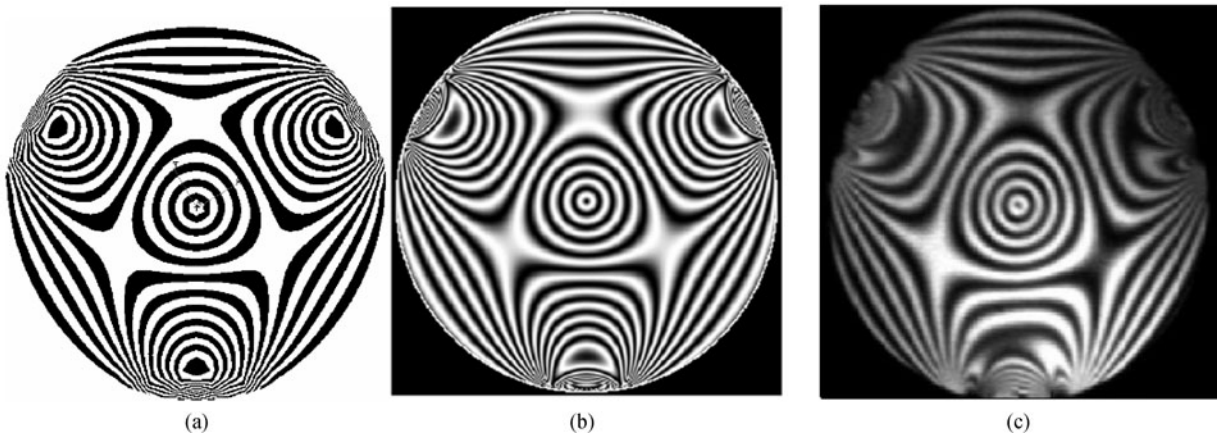

Fig. 4 Comparison of finite element computation (a); analytic solution of Yiannopoulos [12] (b); and experimental image (c), showing contours of equal half wave retardance for trigonally-stressed optical element

with one adapted from the theory of Yiannopoulos [12]. The bright contours show lines of equal half-wave retardance.

For comparison, we show an experimental image of a window illuminated with right circular polarization and analyzed with a left circular analyzer, highlighting the regions of half wave retardance. The equally spaced rings near the center indicate that, in this region, the magnitude of the retardance is increasing linearly with radius but is nearly independent of the azimuth. Figure 5 shows a similar side by side comparison (in simulation) of three windows, in which the number of regions of applied force (the order of the symmetry of the force) of $m = 3$, 4 and 5. The plot shows the absolute retardance as a function of radius for each case. It is clear, both from the spacing of the rings as well as the shape of the retardance function, that the birefringence near the center of the window is proportional to the radius ρ. Since the direction of principal stresses must follow the symmetry, we can infer that the local fast axis will have an orientation. For trigonal ($m = 3$) symmetry, this yields a space-variant Jones matrix as follows:

$$\boldsymbol{J} = \cos\left(\frac{c\rho}{2}\right)\boldsymbol{I} + \mathrm{i}\sin\left(\frac{c\rho}{2}\right)\boldsymbol{P}(-\phi), \tag{2}$$

where $\boldsymbol{I}$ represents the identity matrix and $\boldsymbol{P}$ the pseudorotation matrix:

$$\boldsymbol{P}(\phi) = \begin{bmatrix} \cos\phi & \sin\phi \\ \sin\phi & -\cos\phi \end{bmatrix}.$$

In each case, the orientation of the window is chosen, so

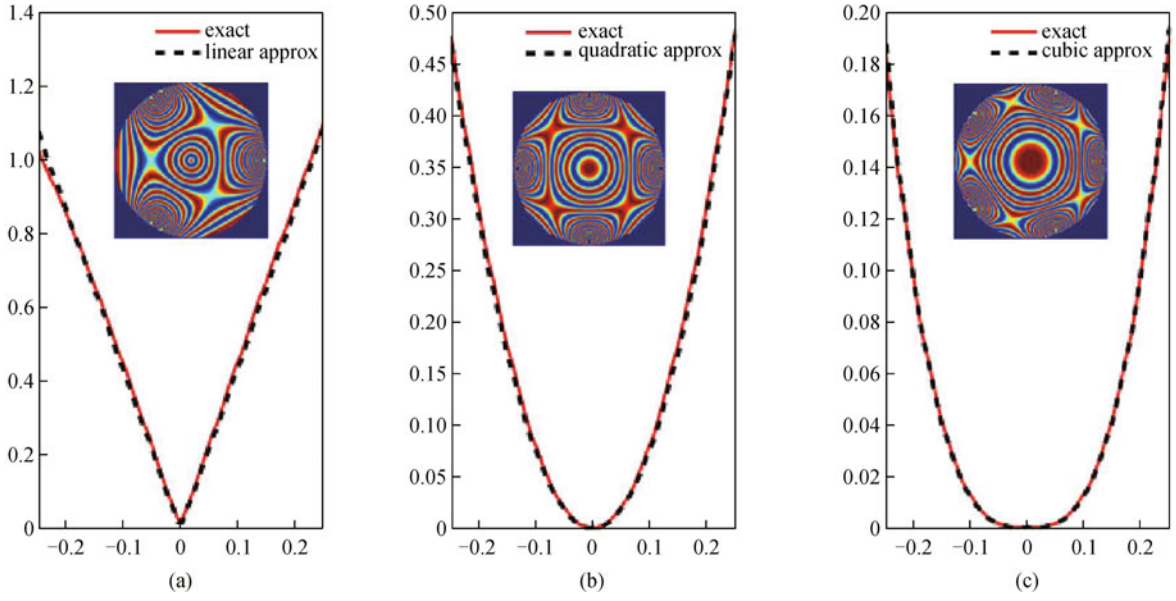

Fig. 5 Retardance (normalized) as function of radius for $m = 3$, 4, and 5 (a, b and c). The insets show the contours of equal retardance based on the analytic model of Iannopolis

that one of the points of contact aligns with the x-axis. A rotation of the window by ϕ_0 simply adds a fixed phase to the argument of $\boldsymbol{P}$.

When illuminated with circular polarization, the transmitted light can be represented by a cosine modulation of the incident polarization superimposed with a vortex that is sinusoidally modulated. So, an incident beam that is left hand circular produces a transmitted polarization distribution:

$$\hat{\boldsymbol{e}}_{\text{out}} = \cos\left(\frac{c\rho}{2}\right)\hat{\boldsymbol{e}}_{\text{L}} + \text{isin}\left(\frac{c\rho}{2}\right)\text{e}^{-\text{i}\phi}\hat{\boldsymbol{e}}_{\text{R}}. \quad (3)$$

The presence of the phase vortex can be readily verified by an interferometric test, in which the window is placed in one arm of a Twyman-Green interferometer as shown in Fig. 6. Figure 7 shows an example of an interferogram obtained from the vortex portion of the transmitted beam along with a phase and amplitude map recovered using a Fourier analysis of the fringe pattern.

If we examine the circular contour corresponding to exactly one half-wave of retardance, the Jones matrix now has the form (neglecting the global phase):

$$\boldsymbol{J}_{1/2} = \boldsymbol{P}(-\phi).$$

When followed by a half wave plate oriented at angle θ, the Jones matrix for the window half waveplate combination is

$$\boldsymbol{J} = \begin{bmatrix} \cos 2\theta & \sin 2\theta \\ \sin 2\theta & -\cos 2\theta \end{bmatrix} \begin{bmatrix} \cos\phi & \sin\phi \\ \sin\phi & -\cos\phi \end{bmatrix}$$

$$= \begin{bmatrix} \cos(\phi - 2\theta) & \sin(\phi - 2\theta) \\ -\sin(\phi - 2\theta) & \cos(\phi - 2\theta) \end{bmatrix} = \boldsymbol{R}(\phi - 2\theta),$$

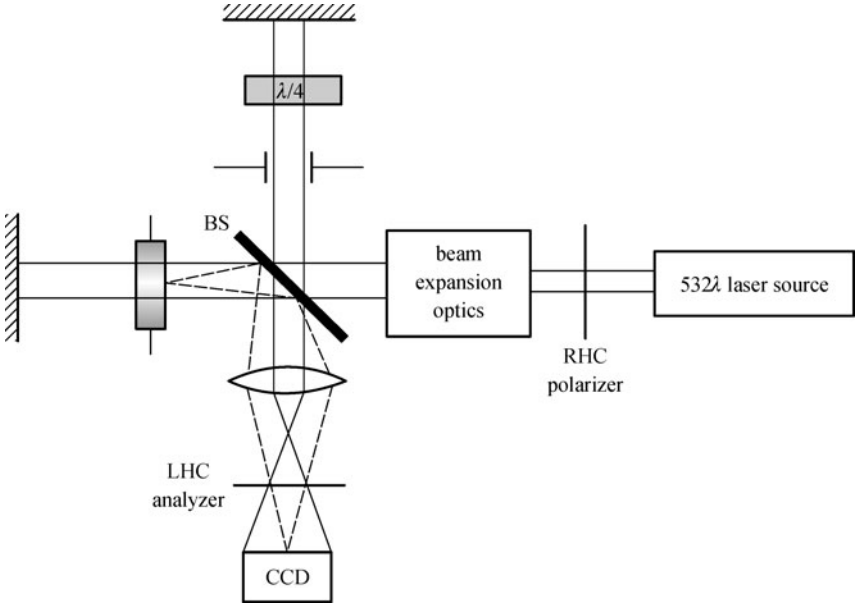

Fig. 6 Twyman Green interferometer for characterizing phase vortex. LHC: left hand circular, RHC: right hand circular

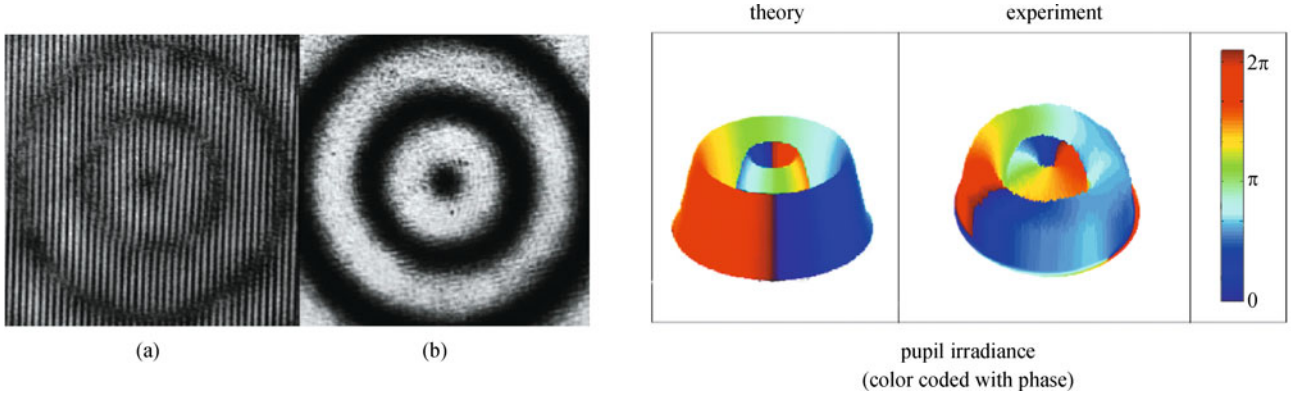

Fig. 7 Left: (a) Interferogram of phase vortex; (b) irradiance of vortex. Right: Reconstructed phase of vortex obtained by Fourier analysis of interferogram

where $\boldsymbol{R}$ denotes the (clockwise) rotation operator. For $\theta = 0$ and an x-polarized input, the output would be an azimuthally polarized field; $\theta = \pi/4$ yields a radially polarized output.

3 Propagation and focusing

We consider two cases of interest: 1) When the window is placed in the pupil plane of a low numerical aperture optical system, in which the usual rules of Fourier optics apply; 2) When a highly stressed window has many rings illuminated and the field propagates in free space. The two cases are illustrated in Fig. 8.

We suppose that the coordinates of the window can be expressed in normalized units, such that $\rho = 1$ corresponds to the edge of the pupil of the optical system. The stress parameter c then represents the phase retardance at the edge of the pupil. Thus, if the pupil diameter is equal to that of the first dark ring, $c = \pi$. Midway through the first bright ring, $c = 2\pi$, and so on, with the radius of each dark ring corresponding to a pupil with a stress parameter that is an odd multiple of π.

If the window is illuminated with a circularly polarized Gaussian beam, whose waist approximately matches the central lobe, the transmitted beam approximates the superposition of a Gaussian central beam having the primary polarization and an outer annulus (a vortex beam) of orthogonal polarization that approximates a LaGuerre-Gauss beam. This was studied in some detail by Beckley et al. [13], in which they showed a set of analytical propagation laws governing the polarization in the focal region. Of particular interest is that any cross section of the focal region encompasses all possible polarization states,

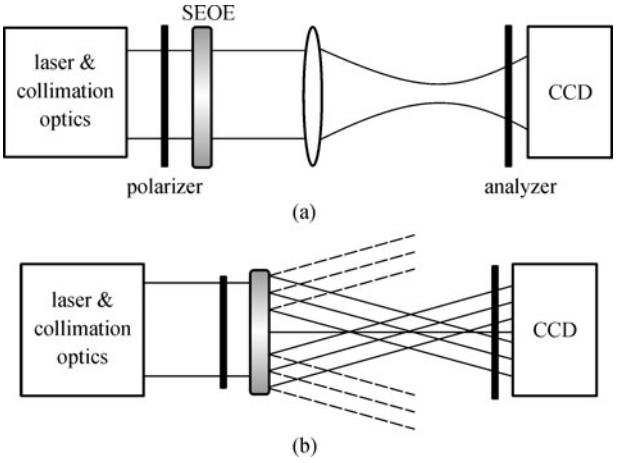

Fig. 8 (a) Arrangement for examining effects of stressed window apodization in focal region of lens; (b) arrangement for studying propagation of Bessel-like beams transmitted through high-stress window

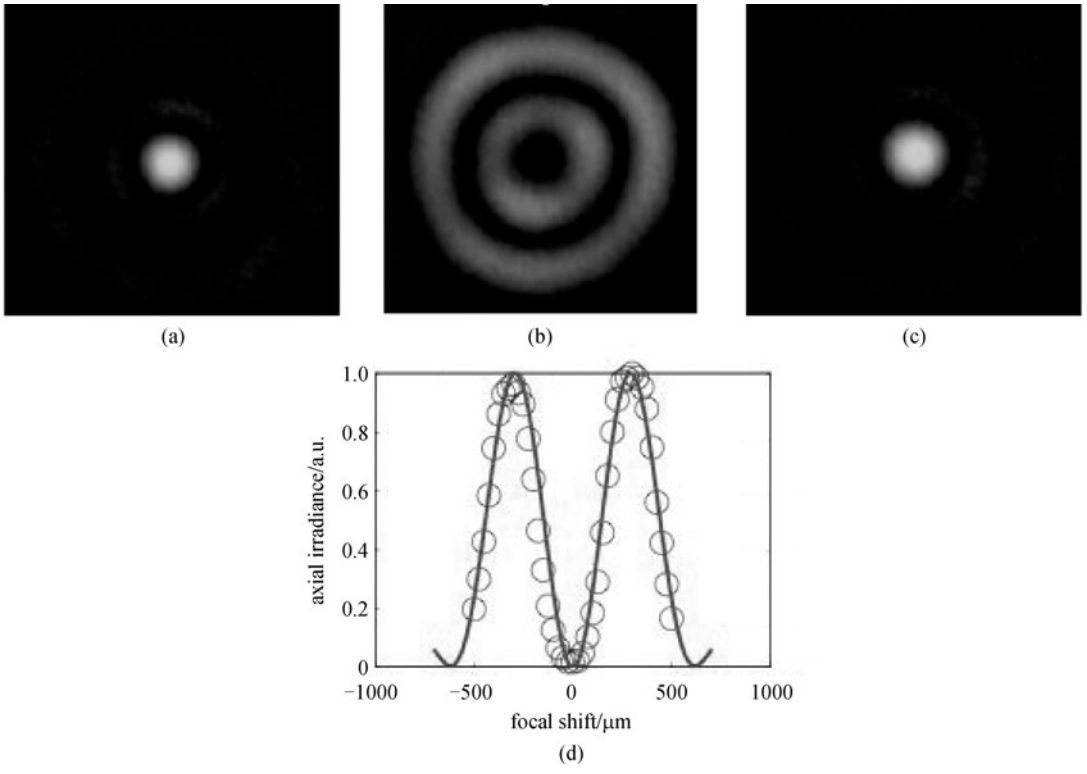

Fig. 9 Focal splitting from threefold stress at low numerical aperture. (a–c) show the point spread functions at the inner focus, the paraxial focus, and the outer focus; (d) shows a comparison of the measured axial irradiance with that calculated from a numerical estimate based on the power law model

and that the physical location of any given polarization state may be related to its location on the Poincare sphere by a stereographic mapping.

As the aperture increases to $c = 2\pi$, there is an axial splitting of the focal region. This effect was first observed by Spilman and Brown [9], who compared the axial irradiance with that predicted by the power law model. Figures 9(a)–9(c) shows the through focus image of a point source of circular polarization, with two axially separated focal spots and an annular region at the paraxial focus. Spilman and Brown suggested several models by which the focal splitting could be estimated; here, we offer a simplified picture that is consistent with a zone plate concept.

We first consider only the primary polarization, which passes through the window with a cosine apodization. The primary significance of this apodization is that the outer ring will be out of phase with the central lobe. Thus, contributions from inner and outer regions that would normally add in phase at the paraxial focus are now out of phase, yielding a null in the region close to the paraxial focus. An off axis shift in any direction will eventually lead to a constructive interference condition, yielding the rings in the paraxial image plane and the two separated axial foci. Figure 10 shows the behavior of the focal splitting (evaluated in terms of the axial irradiance) for increasing stress, as the order of the symmetric stress increases.

We now consider the case in which light propagates through a highly stressed window without a lens (in this case c is many multiples of π) in the case of circularly polarized illumination. As before, the primary (incident) polarization is transmitted with an apodization of $\cos(c\rho/2)$ and the orthogonal polarization transmits as $\sin(c\rho/2)$ (A complementary irradiance patter with a phase vortex.) Beckley et al. [14] showed that each of these propagates in a manner similar to an apodized Bessel beam that features a tight central lobe over an axial region much longer than the depth of focus of a Gaussian beam of equivalent size (Fig. 11).

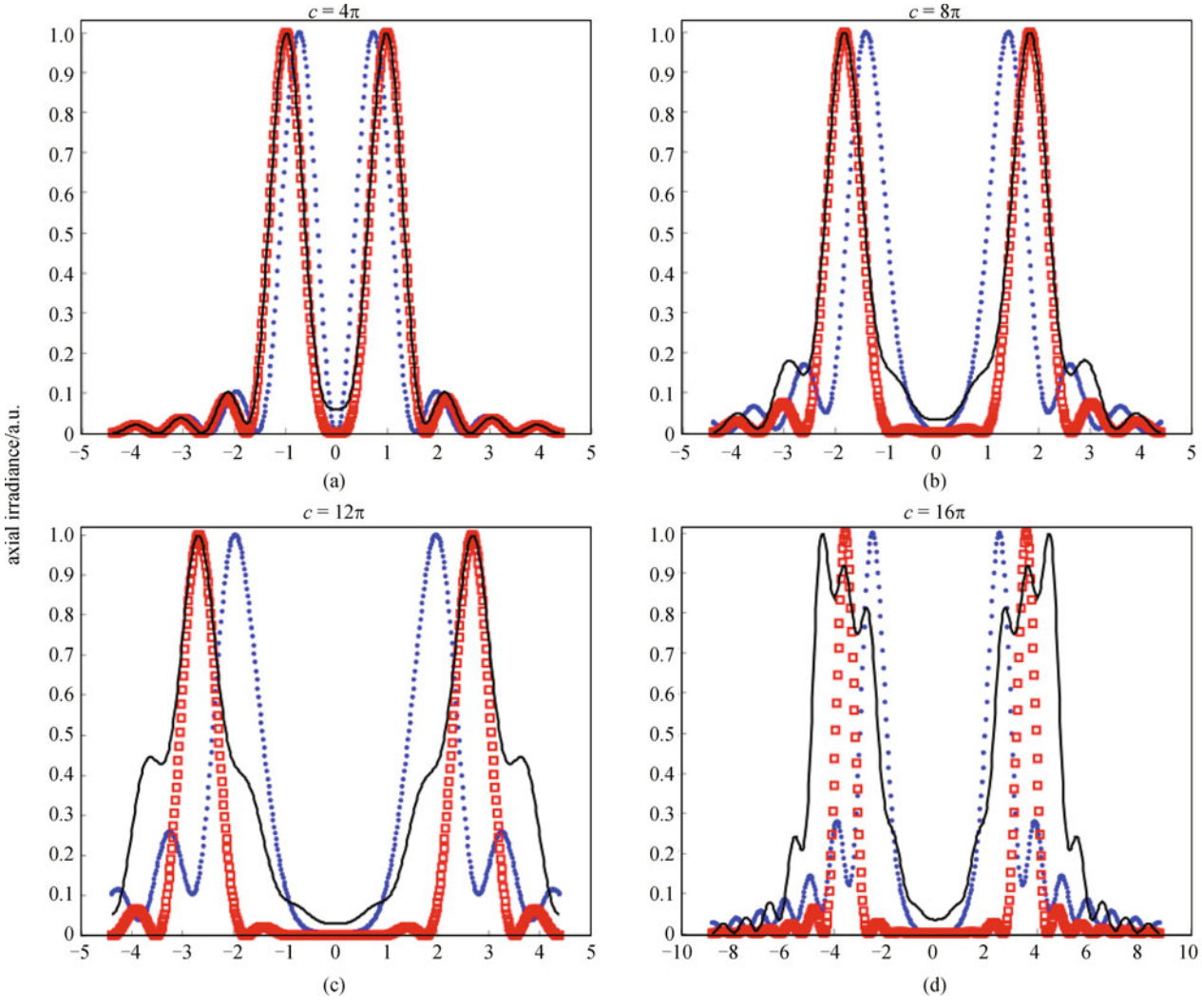

Fig. 10 Axial irradiance patterns for a range of stress parameters c. (a) $c = 4\pi$; (b) $c = 8\pi$; (c) $c = 12\pi$; (d) $c = 16\pi$. Because the focal splitting expands in proportional to the stress, the highest stress case has an expanded horizontal scale

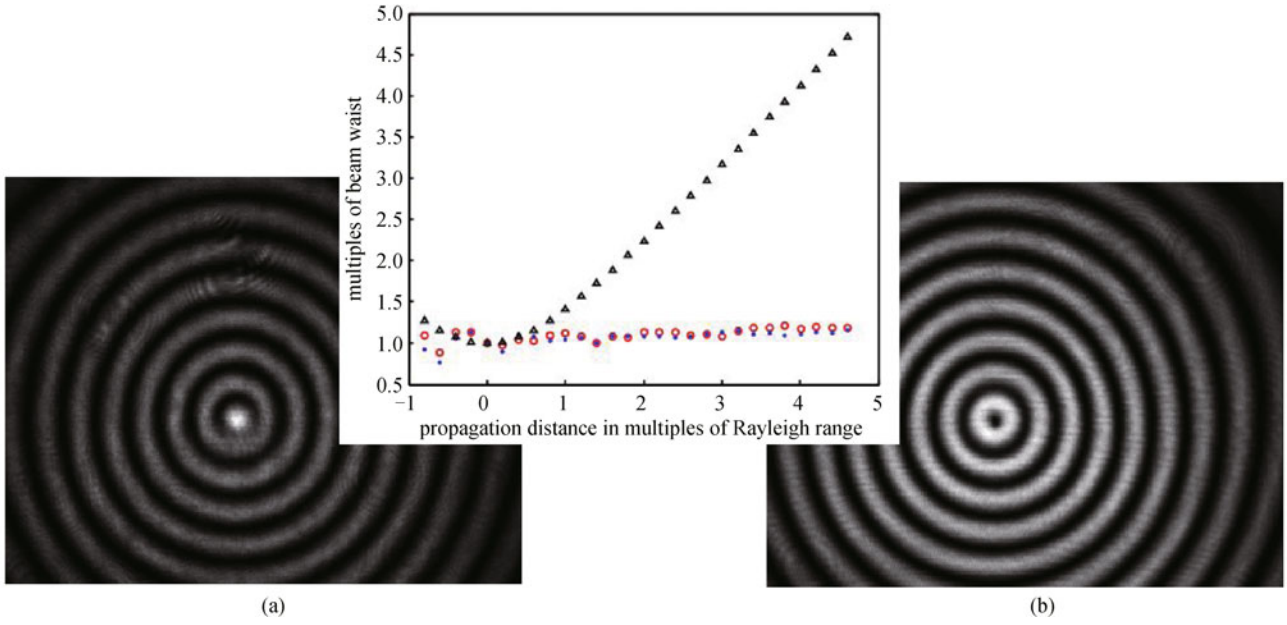

Fig. 11 Photographs showing irradiance pattern of non-vortex (a) and vortex (b) Bessel-like beams. The inset shows a measurement of the central lobe under propagation compared with a Gaussian beam of equivalent size

4 Star test polarimetry

We now explore the use of stress engineered optical elements for polarimetric applications that was suggested by Beckley and Brown [15] and refined by Ramkhalawon et al. [16]. The idea is to use the available range of values for retardance and orientation in a stressed window to provide polarization diversity in the image sufficient to recover the Stokes parameters. Here, we focus on a particular version of polarization analysis in an image plane that we call star test polarimetry. The concept is based on the use of a polarization dependent point spread function; if a stressed window is illuminated (in the pupil plane) with a uniform but unknown state of polarization

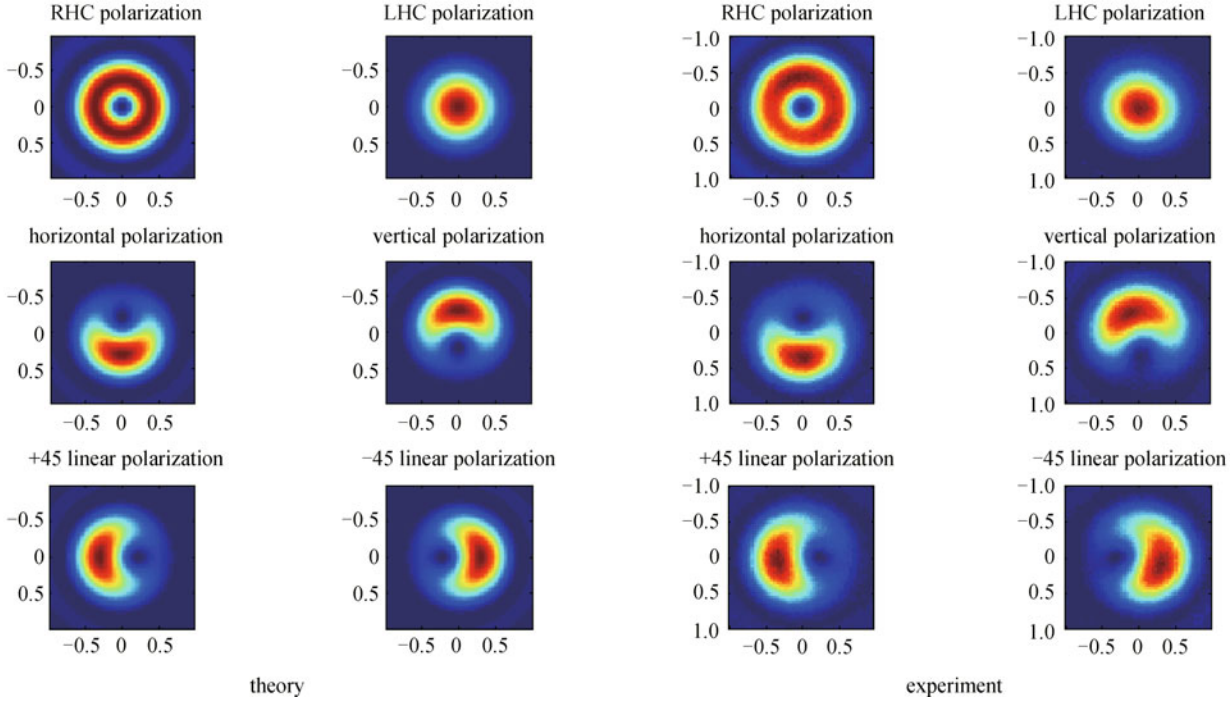

Fig. 12 Polarization dependent point spread functions using stress engineered optical element. In each case, the input state of polarization is listed above the image. RHC (LHC) polarizations refer to right (left) hand circular polarizations

Table 1 Representative Stokes measurements using star test polarimetry according to calibration procedure in Ref. [16]

input states	S_1	S_2	S_3	error/rad	DoP
horizontal	0.9712	0.0094	0.0204	0.0232	0.9715
vertical	−0.9881	0.0037	0.0186	0.0192	0.9883
+45 linear	0.0100	0.9781	−0.0095	0.0141	0.9782
−45 linear	0.0051	−0.9758	0.0094	0.0109	0.9758
right hand circular	0.0000	0.0000	1.0000	0	1.0000
left hand circular	0.0000	0.0000	−1.0000	0	1.0000
elliptical	−0.4056	0.7529	−0.5040	0.0319	0.9927

Note: The error column refers to the absolute difference in between the normalized Stokes 3-vector and that measured using a commercial (Thorlabs^{TM}) polarimeter

and followed by an analyzer, the shape of the point spread function will have a signature unique to that particular state of polarization. Figure 12 shows an example of this, in which a stressed window is followed by a left hand circular analyzer and illuminated with a range of polarization states.

The calibration and measurement procedures for such a system are described in some detail in Ref. [16]. Table 1 shows a sample compilation of measurements from fully polarized beams of light, listing the difference when compared to a commercial polarimeter.

5 Conclusions

Stress engineering is a promising tool for situations requiring static, stable elements for polarization apodization, including applications such as focus shaping and vortex beam generation. We have also shown how the concept can be applied to quantitative polarimetry, in which a single image of a point spread function can yield an accurate estimate of the Stokes parameters of the incident light.

Acknowledgements This work was supported in part by the National Science Foundation (PHY-1068325), the Semiconductor Research Corporation, Rochester Precision Optics, and KLA-Tencor Corporation.

References

1. Greene P, Hall D. Properties and diffraction of vector Bessel-Gauss beams. Journal of the Optical Society of America A, 1998, 15(12): 3020–3027
2. Zhan Q. Cylindrical vector beams: from mathematical concepts to applications. Advances in Optics and Photonics, 2009, 1(1): 1–57
3. Brown T G. Unconventional polarization states: beam propagation, focusing, and imaging. Progress in Optics, 2011, 56: 81–129
4. Sheppard C J R, Saghafi S. Transverse-electric and transverse-magnetic beam modes beyond the paraxial approximation. Optics Letters, 1999, 24(22): 1543–1545
5. Sheppard C J R, Choudhury A. Annular pupils, radial polarization, and superresolution. Applied Optics, 2004, 43(22): 4322–4327
6. Dorn R, Quabis S, Leuchs G. Sharper focus for a radially polarized light beam. Physical Review Letters, 2003, 91(23): 233901
7. Youngworth K S, Brown T G. Focusing of high numerical aperture cylindrical-vector beams. Optics Express, 2000, 7(2): 77–87
8. Youngworth K S, Brown T G. Inhomogenous polarization in scanning optical microscopy. In: Proceedings of SPIE 3919, Three-Dimensional and Multidimensional Microscopy: Image Acquisition Processing VII. 2000, 75
9. Spilman A K, Brown T G. Stress-induced focal splitting. Optics Express, 2007, 15(13): 8411–8421
10. Spilman A K, Brown T G. Stress birefringent, space-variant wave plates for vortex illumination. Applied Optics, 2007, 46(1): 61–66
11. Spilman A K, Beckley A M, Brown T G. Focal splitting and optical vortex structure induced by stress birefringence. In: Proceedings of SPIE 6667, Current Developments in Lens Design and Optical Engineering VIII. 2007, 66670I
12. Yiannopoulos A Ch. A general formulation of stress distribution in cylinders subjected to non-uniform external pressure. Journal of Elasticity, 1999, 56(3): 181–198
13. Beckley A M, Brown T G, Alonso M A. Full Poincaré beams. Optics Express, 2010, 18(10): 10777–10785
14. Beckley A M, Alonso M A, Brown T G.Diffraction free stokes distributions in a full poincare beam. In: Proceedings of Frontiers in Optics, Optical Society of America Technical Digest (CD). 2010, FThN2
15. Beckley A M, Brown T G. Pupil polarimetry using stress-engineered optical elements. In: Proceedings of SPIE 7570. Three-Dimensional and Multidimensional Microscopy: Image Acquisition XVII. 2010, 757011
16. Ramkhalawon R D, Beckley A M, Brown T G. Star test polarimetry using stress-engineered optical elements. In: Proceedings of SPIE 8227, Three-Dimensional and Multidimensional Microscopy: Image Acquisition and Processing XIX. 2012, 82270Q